Wind Direction Estimation by Deconvolution of GNSS Delay–Doppler Maps: A Simulation Analysis

Generoso Giangregorio [ID], Carmela Galdi [ID], *Member, IEEE*, and Maurizio di Bisceglie [ID], *Member, IEEE*

Abstract—Signatures of directional wind waves are discovered after deconvolution of delay–Doppler maps in Global Navigation Satellite System reflectometry from space. The simulation study and the proposed algorithm demonstrate that wind direction can be, in principle, retrieved in the presence of thermal noise and speckle. The method is based on a least squares approach where an overdetermined system of equations is solved with respect to wind direction assuming that sea surface mean square slopes have been previously estimated. Performance is assessed on simulated data, where the system geometry is defined according to a realistic ocean scattering scenario. The algorithm accuracy is investigated with respect to different sizes of the observable and with respect to speckle and thermal noise.

Index Terms—Deconvolution, Global Navigation Satellite System (GNSS) reflectometry, simulation, wind direction estimation.

I. INTRODUCTION

THE theoretical background developed in [1] as well as the evidence of measurable quantities related to the ocean surface have generated a rich amount of literature addressing the problem of ocean wind speed estimation from reflected Global Navigation Satellite System (GNSS) signals. The most widely accepted and validated wind-speed retrieval methods are based on the development of a geophysical model function; they are currently used operationally for the generation of CYclone Global Navigation Satellite System (CYGNSS) [2]–[4] and TDS-1 [5], [6] products. Other attracting approaches have been developed in [7]–[10], where the basis is a parametric retrieval from the delay–Doppler map (DDM) observable. A wind direction product has not been considered up to now because the sensitivity of the ocean retrieved signal to wind direction appears to be very weak. The topic was firstly addressed with airborne receivers in [11] and [12], where wind-induced anisotropy in the aircraft measured waveform is investigated and sensitivity of wind direction measurements to system parameters is analyzed. In [13], the predicted elongation of the glistening zone is exploited through a least squares (LS) approach for simultaneous estimation of wind speed and wind direction. A measure of asymmetry of the DDM power distribution along

the Doppler direction was introduced in [14]. After assessment with simulated data, the method was validated with airborne real data.

The first analysis with TDS-1 satellite data was developed in [15] using an LS approach in 2-D also validated with *in situ* data. The DDM in this case was generated with 18 s incoherent integration time. More recently, the wind direction effects in the region near specular scattering have been investigated showing that wind direction dependence in spaceborne GNSS-R should be only captured away from the specular region [16]. A feasibility study on simulated data was presented in [17], where two metrics were proposed to investigate DDM changes induced by wind direction. A different setup was presented in [18], where a low-altitude backward geometry is considered for matching the theoretical model to measurements.

The starting point of this study is the preliminary estimation of the scattered power function (SPF) through deconvolution. It is based on the DDM model as 2-D convolution between the SPF and the square modulus of the ambiguity function. The ambiguity function depends on the transmitted pseudorandom noise (PRN) code and determines the final spatial resolution of the DDM observable, whereas the SPF contains all useful information about the distribution of the scattered power in the glistening zone. A widely assessed procedure for deconvolution is based on constrained least square (CLS) approach. It provides a good compromise between precision and complexity [19] and was used for the first time in [20] for deconvolution of DDMs with application to oil slick detection and cyclone sensing.

After deconvolution, replacing the probability density function (pdf) of the sea surface slopes with its first-order Taylor approximation around the specular point, the SPF can be evaluated for each point of the DDM. The resulting overdetermined system of equations is solved in the LS sense. Performance has been assessed on simulated data, generated according to a CYGNSS track geometry, for several values of wind speed and DDM size.

The rest of this article is organized as follows. In Section II, the deconvolution process is presented and some practical suggestions to minimize errors are discussed. In Section III, the retrieval algorithm is presented. The assessment of the algorithm on simulated DDM is discussed in Section IV. Conclusion and final remarks are reported in Section V.

II. DECONVOLUTION OF DDMS

The DDM can be modeled as the 2-D convolution [10]

$$\mathbb{E}\left[|Y(\tau, f)|^2\right] = |\chi(\tau, f)|^2 * \xi(\tau, f) + \mathbb{E}\left[|N(\tau, f)|^2\right] \quad (1)$$

where the symbol $*$ indicates the 2-D convolution operator, $\mathbb{E}$ denotes statistical expectation, $\chi(\tau, f)$ is the ambiguity function of the transmitted PRN waveform, $\xi(\tau, f)$ is the SPF in the delay–Doppler domain, and $N(\tau, f)$ is the thermal noise at the correlator output. Due to the ambiguity, the SPF in the delay–Doppler domain is the sum of two terms corresponding to different scattering areas [21], [22]

$$\xi(\tau, f) = \xi_1(\tau, f) + \xi_2(\tau, f) \quad \text{with}$$

$$\xi_i(\tau, f) = g_i(\tau, f) P_{\zeta_x \zeta_y} \left(\frac{q_{xi}(\tau, f)}{q_{zi}(\tau, f)}, \frac{q_{yi}(\tau, f)}{q_{zi}(\tau, f)}; \sigma_u, \sigma_c, \theta \right)$$

$$\text{and} \quad g_i(\tau, f) = \frac{T^2 \mathscr{D}_i^2 |\mathscr{R}_i|^2}{4 R_i^2 R_{0i}^2} \frac{|\boldsymbol{q}_i|^4}{q_{zi}^4} |J_i(\tau, f)|, \quad i = 1, 2. \quad (2)$$

Here, the index i denotes the two possible solutions for each delay–Doppler cell, with $\xi_2 = 0$ for points lying on the ambiguity free line. The symbol T denotes the coherent integration time, $\mathscr{D}$ is the receiving antenna pattern, $\mathscr{R}$ is the Fresnel reflection coefficient, $\boldsymbol{q} = (q_x, q_y,$ and $q_z)$ is the scattering vector, and R and R_0 are the range from the surface point to the receiver and from the transmitter to the surface point, respectively. $J(\tau, f)$ is the Jacobian of the mapping transformation, $P_{\zeta_x \zeta_y}$ is the joint pdf of the sea surface slopes, σ_u^2 and σ_c^2 are the up-wind and cross-wind mean square slopes, respectively, and θ is the wind direction.

From (1), the function $\xi(\tau, f)$ can be obtained as a 2-D deconvolution. With respect to a classical recovery process in additive noise, here an additional degradation arises from the consideration that DDMs are cropped after on-board processing, for obvious reasons of data transmission compactness and, therefore, (1) is available only in a domain of limited size. The error due to DDM cropping can be reduced as in [10]. Therefore, before deconvolution, the mean noise floor is removed by subtraction from the DDM and, similarly, the noise floor is removed from the square modulus of the ambiguity function. Because the DDM size is much larger than the main lobe of the ambiguity function, the deconvolution provides, with good approximation, a cropped version of the SPF with the same size of the DDM.

In the discrete time, the CLS is a well-known approach for signal deconvolution in the presence of additive disturbance [19]. The rationale of CLS is to minimize the roughness of the function with a constraint on the deconvolution error. The discrete-time Laplacian operator provides a measure of the roughness; therefore the solution $\widehat{\xi}$ is obtained by minimizing the Laplacian of the SPF with the constraint that the norm of the deconvolution error $\mathbb{E}[|Y(n,m)|^2] - |\chi(n,m)|^2 * \widehat{\xi}(n,m)$ is equal to the norm of the noise power $\mathbb{E}[|N(n,m)|^2]$. The expression of the deconvolved SPF in the frequency domain, where the variables (n, m) have been omitted for shortness, is

$$\mathscr{F}[\widehat{\xi}] = \frac{\mathscr{F}[|\chi|^2]^*}{|\mathscr{F}[|\chi|^2]|^2 + \gamma |\mathscr{F}[p]|^2} \mathscr{F}[\mathbb{E}[|Y|^2]] \quad (3)$$

where $\mathscr{F}$ denotes Fourier transform, γ is the Lagrange multiplier, and p is the Laplacian filter in 2-D. The value of the Lagrange multiplier that satisfies the constraint can be found using the iterative procedure proposed in [19]. It is worth to note that γ is a
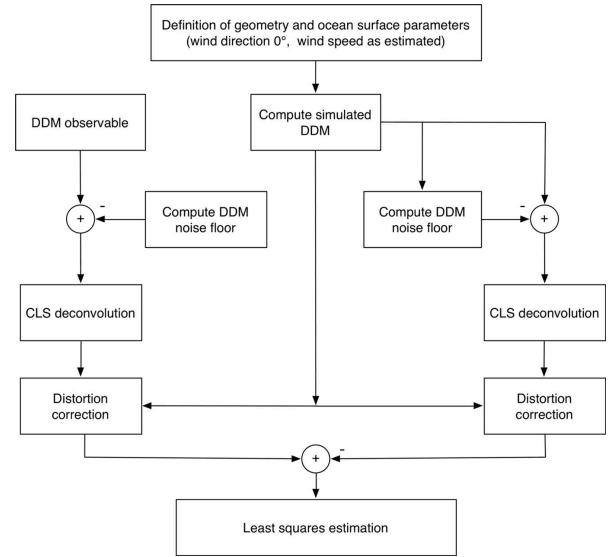

Fig. 1.	Scheme of the wind-direction retrieval algorithm.

smoothing factor whose value affects the noise reduction, on one side, and the signal distortion on the other side. For $\gamma = 0$, the deconvolution function reduces to the inverse filter $1/\mathscr{F}[|\chi|^2]$, whereas for increasing values of γ, more noise is filtered out but fine signal details are blurred more severely. To improve robustness against filter distortion, a postprocessing strategy was proposed in [20], where the aim is the retrieval of the scattering coefficient in GNSS-R ocean mapping. Distortion correction has some impact on the optimum choice of the Lagrange multiplier, that is no longer entirely determined by the energy constraint. The optimum choice of the Lagrange multiplier is analyzed in Section III-C.

III. WIND-DIRECTION RETRIEVAL

In principle, after deconvolution of the DDM, wind direction and wind speed can be estimated by nonlinear fitting with the joint pdf of the sea surface slopes. This procedure, although theoretically applicable, is too sensitive to deconvolution errors and is computationally demanding. Therefore, we will proceed in a pretty different way: 1) to improve robustness with respect to deconvolution errors, the estimation is carried out on the difference between SPF obtained from the data and SPF obtained from a simulated map; and 2) to reduce the computational burden, the system of nonlinear equations is linearized at the first order around the specular point and solved at LS.

The algorithm is depicted in the scheme of Fig. 1 along with additional comments provided hereafter.
1) A prototype DDM is simulated using platforms and geometry, which accurately match the real acquisition scenario. The sea surface mean square slopes are assumed estimated in a previous step, whereas the wind direction is set to $0°$.
2) In order to reduce the error due to DDM cropping, the noise floor is estimated and removed from both DDM observable and prototype DDM.
3) The SPF is retrieved from the DDM observable and from the prototype DDM via deconvolution. In both cases
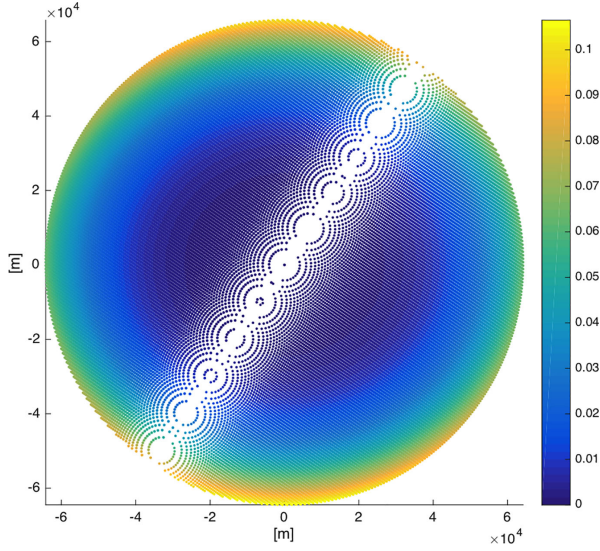
Fig. 2. Relative error for the first-order Taylor approximation of the slopes pdf around the specular direction. Axes are centered in the specular point and the extension of the observed surface corresponds to Doppler frequency in the range ±5000 Hz and delay (0–15) chips. Wind speed and wind direction are 5 m/s and 0°, respectively.

the distortion is corrected as in [20]. The deconvolved SPF contains similar artifacts in the two cases, therefore additive residuals are canceled out by computing difference between SPFs. The remaining features can be reasonably attributed to direction-dependent scattering from wind waves viewed after remapping in the delay–Doppler frame. The directional wind effects are mapped in nonlinear form into the 2-D slopes pdf for each delay–Doppler resolution cell, such that an overdetermined nonlinear system of equations can be defined and solved in terms of the wind direction.

4) The slopes pdf is linearized by retaining the terms of the Taylor expansion up to the first order. The system of equations, one for each delay–Doppler resolution cell, can be solved in the LS sense.

A. First-Order Approximation of the Slopes pdf

The slopes pdf $P_{\zeta_x \zeta_y}(\cdot)$ is usually assumed as Gaussian with covariance matrix $\mathbf{C} = \mathbf{R}(\theta)\mathbf{\Lambda}(\sigma_u^2, \sigma_c^2)\mathbf{R}^T(\theta)$ where $\mathbf{R}$ is the rotation matrix in 2-D and $\mathbf{\Lambda}$ is a diagonal matrix. In the delay–Doppler region where full DDMs are usually represented, i.e., ±5000 Hz for Doppler frequency and (0–15) chips for delay, the slopes pdf is smooth and can be well approximated by its first-order Taylor expansion around specular direction $\mathbf{z}^T = (u, v) = -(q_x/q_z, q_y/q_z) = \mathbf{0}$ as

$$\widetilde{P}_{\zeta_x \zeta_y}(\mathbf{z}) \simeq \frac{1}{2\pi\sigma_u\sigma_c}\left[1 - \frac{1}{2}\mathbf{z}^T\mathbf{C}^{-1}\mathbf{z}\right]. \quad (4)$$

The relative error $(P_{\zeta_x \zeta_y} - \widetilde{P}_{\zeta_x \zeta_y})/P_{\zeta_x \zeta_y}$ is shown in Fig. 2 for 5 m/s wind speed and wind direction aligned with the reference coordinates ($\theta = 0°$). In order to provide a realistic evaluation of the goodness of the pdf approximation, the points represented in the figure are obtained starting from equispaced

delay–Doppler samples in a typical acquisition geometry and reprojected into the spatial domain. Furthermore, the error in the figure is represented as a function of the spatial coordinates given in meters starting from the specular point. For points in the range ±5000 Hz in Doppler and (0–15) chips in delay (the size of the DDM), the relative error is below 10% and for most of the points is below 5%.

B. Wind Direction Estimation

Denote as $\widehat{\xi}_o$ and $\widehat{\xi}_p$ the deconvolved SPF observable and SPF prototype, respectively. According to (2), we have

$$\widehat{\xi}_o(\tau, f) - \widehat{\xi}_p(\tau, f)$$
$$= \sum_{i=1,2} g_i(\tau, f)\left[P_{\zeta_x \zeta_y}(\mathbf{z}_i(\tau, f); \sigma_u, \sigma_v, \theta)\right. \quad (5)$$
$$\left. - P_{\zeta_x \zeta_y}(\mathbf{z}_i(\tau, f); \sigma_u, \sigma_v, 0)\right].$$

The difference between slopes pdf in (5) can be approximated as in (4) and, after some manipulations, can be expressed as

$$P_{\zeta_x \zeta_y}(\mathbf{z}(\tau, f); \sigma_u, \sigma_v, \theta) - P_{\zeta_x \zeta_y}(\mathbf{z}(\tau, f); \sigma_u, \sigma_v, 0)$$
$$= \frac{1}{8\pi\sigma_u\sigma_c}\left(\frac{1}{\sigma_u^2} - \frac{1}{\sigma_c^2}\right)\mathbf{z}^T\mathbf{K}(\theta)\mathbf{z} \quad (6)$$

with

$$\mathbf{K}(\theta) = \begin{bmatrix} 1 - \cos 2\theta & -\sin 2\theta \\ -\sin 2\theta & -1 + \cos 2\theta \end{bmatrix}. \quad (7)$$

After rearranging (5), we get

$$\frac{8\pi\sigma_c^3\sigma_u^3}{\sigma_u^2 - \sigma_c^2}\left[\widehat{\xi}_o(\tau, f) - \widehat{\xi}_p(\tau, f)\right]$$
$$= \sum_{i=1,2} g_i(\tau, f)\left[(u_i^2(\tau, f) - v_i^2(\tau, f))(1 - \cos 2\theta)\right.$$
$$\left. - 2u_i(\tau, f)v_i(\tau, f)\sin 2\theta\right]. \quad (8)$$

Equation (8) can be specified for each point of the delay–Doppler grid, say (τ_j, f_j), $j = 1, \ldots N$. In the hypothesis of constant wind field, a nonlinear system of equations in the variable θ is obtained, with constant terms, for $j = 1, \ldots, N$

$$b_j = \sum_{i=1,2} g_i(\tau_j, f_j)(u_i^2(\tau_j, f_j) - v_i^2(\tau_j, f_j))$$
$$- \frac{8\pi\sigma_c^3\sigma_u^3}{\sigma_u^2 - \sigma_c^2}\left[\widehat{\xi}_o(\tau_j, f_j) - \widehat{\xi}_p(\tau_j, f_j)\right] \quad (9)$$

and coefficients

$$a_{j1} = \sum_{i=1,2} g_i(\tau_j, f_j)(u_i^2(\tau_j, f_j) - v_i^2(\tau_j, f_j))$$
$$a_{j2} = \sum_{i=1,2} 2g_i(\tau_j, f_j)(u_i(\tau_j, f_j)v_i(\tau_j, f_j)). \quad (10)$$

The nonlinear system is highly overdetermined and can be solved in the LS sense

$$\widehat{\theta} = \arg\min_\theta ||\mathbf{A}\boldsymbol{x}(\theta) - \mathbf{b}||^2 \quad (11)$$

where $\boldsymbol{x}(\theta) = [\cos 2\theta \ \sin 2\theta]^T$, and the matrix of coefficients $\mathbf{A}$ and the constant terms vector $\mathbf{b}$ are

$$\mathbf{A} = \begin{bmatrix} a_{11} & a_{12} \\ \vdots & \vdots \\ a_{N1} & a_{N2} \end{bmatrix} = \begin{bmatrix} \mathbf{a_1} & \mathbf{a_2} \end{bmatrix} \quad \mathbf{b} = \begin{bmatrix} b_1 \\ \vdots \\ b_N \end{bmatrix}. \quad (12)$$

We provide here two different solutions to the problem: in one case a direct approach is considered by solving the LS problem (11) with respect to θ. This method will be referred to as direct nonlinear LS (DNLS). In the other, it is solved by first finding the LS solution of the linear system with respect to the variables $x_1 = \cos 2\theta, x_2 = \sin 2\theta$, from which the LS solution θ can be derived. This method will be referred to as linear LS (LLS). In the first case, the solution is

$$\widehat{\theta}_{\text{DNLS}} = \underset{\theta \in [0,\pi[}{\arg\min} [\ (||\mathbf{a_1}||^2 - ||\mathbf{a_2}||^2) \cos 4\theta + 2\mathbf{a_1}^T \mathbf{a_2} \sin 4\theta$$

$$+ 4\mathbf{a_1}^T \mathbf{b} \cos 2\theta + 4\mathbf{a_2}^T \mathbf{b} \sin 2\theta] \quad (13)$$

and in the second

$$\widehat{\theta}_{\text{LLS}} = \frac{1}{2} \arctan_2 \frac{\widehat{x}_2}{\widehat{x}_1} \quad (14)$$

where $\widehat{\boldsymbol{x}} = [\widehat{x}_1, \widehat{x}_2]^T$ is the solution of the LLS problem

$$\widehat{\boldsymbol{x}} = \left(\mathbf{A}^T \mathbf{A}\right)^{-1} \mathbf{A}^T \mathbf{b}. \quad (15)$$

It is worth noting that, ideally, the two solutions should be equal because of the invariance of the LS estimation. However, due to possible mismatch and approximation of the model, the relationship between the wind direction θ and the coefficients $\boldsymbol{x}$ could be not accurately described by the expression in (11). Therefore, the direct solution is more precise when the errors in the model are reduced, whereas the second solution is more robust thanks to the introduction of an additional parameter; therefore, it is advantageous when the model becomes too approximated. This is better discussed in the following section.

C. Spatial Resolution

Some discussion is here useful about achievable spatial resolution of wind direction measurements. Wind and wave parameter from DDM observable could be in principle measured within an area that is defined by the intersection of iso-delay and iso-Doppler lines of the delay–Doppler cell [23]. This purely geometric definition is degraded by power spreading across adjacent delay–Doppler cell boundaries due to ambiguity function, by the incoherent averaging, and by the processing used for wind estimation.

Let us consider, now, the effect of deconvolution in our processing scheme. A favorable impact of deconvolution is that the process removes the power spreading due to ambiguity function and the resulting resolution turns out to be close to the theoretical geometric definition. The deconvolution algorithm used in this article introduces, however, two additional effects that can affect resolution. One effect is due to the Laplacian smoothing filter, the other is determined by distortion correction that requires the generation of an additional SPF with constant wind speed over the whole glistening zone. But this constant wind speed, over a quite large area, in general can reduce the accuracy of wind estimation rather than the resolution. As to the overall deconvolution error, it is reasonably small for the chosen value of γ (see Fig. 4 and discussion in Section III-D) and diffused over all SPF cells.

After deconvolution, the estimation algorithm tries to retrieve a constant wind direction by solving a nonlinear system where the number of equations is determined by the size of the SPF. The spatial resolution is ultimately dependent by the spatial extension of the SPF tile used in the estimation algorithm. Performance degrades when the number of samples decreases so a tradeoff between estimation error and spatial resolution must be considered.

Finally, the resolution is also affected by the incoherent integration time and by the average of the estimates over multiple point over the track. If the incoherent integration time is limited to 1 s the spatial resolution is only marginally affected; on the other hand, averaging over multiple track points produces smoothing of the wind-direction retrievals and should be kept as small as possible.

D. Looking Into the Observable

Wind direction estimation is performed on the difference between SPF-observable and SPF-prototype after deconvolution of the parent DDMs. It is instructive to briefly analyze the delay–Doppler features induced by wind direction variations into the difference SPF. A comparison between the ideal SPF difference, obtained from simulated unprocessed SPF prototypes, and SPF difference after deconvolution, is shown in Fig. 3 for three values of wind direction ($\theta = 30°$, $90°$, and $120°$). There is clear evidence that wind direction generates features that are generally nonsymmetric with respect to the zero-Doppler line. It appears that directional wind engraves deep and sharp valleys whose position and orientation are strongly dependent on wind direction. After deconvolution, such signatures persist in the original shape that appears, however, slightly damaged by artifacts. It is reasonable that the artifacts close to the SPF delay edge are due to the finite size of the DDM as they appear for all directions. These arguments suggest that information on wind direction, which is captured in the SPF difference, may be retrieved with reasonable accuracy with the overdetermined LS approach.

Another consideration is useful in order to the determination of the Lagrange multiplier γ. The optimum choice of γ was performed by analyzing the median of the absolute error

$$\epsilon(\tau, f) = |(\widehat{\xi}_o - \widehat{\xi}_p) - (\xi_o - \xi_p)| \quad (16)$$

calculated over all delay and Doppler values. We may recognize that the first term of the error is observable in (5) and the other is the difference between calculated SPF according to (2). It is shown in Fig. 4 that such error exhibits an exponentially decreasing profile versus logarithm of γ. For values of γ less than 10^2, the behavior is rapidly decreasing, whereas for values of γ larger than 10^4, there is little dependence on values of the
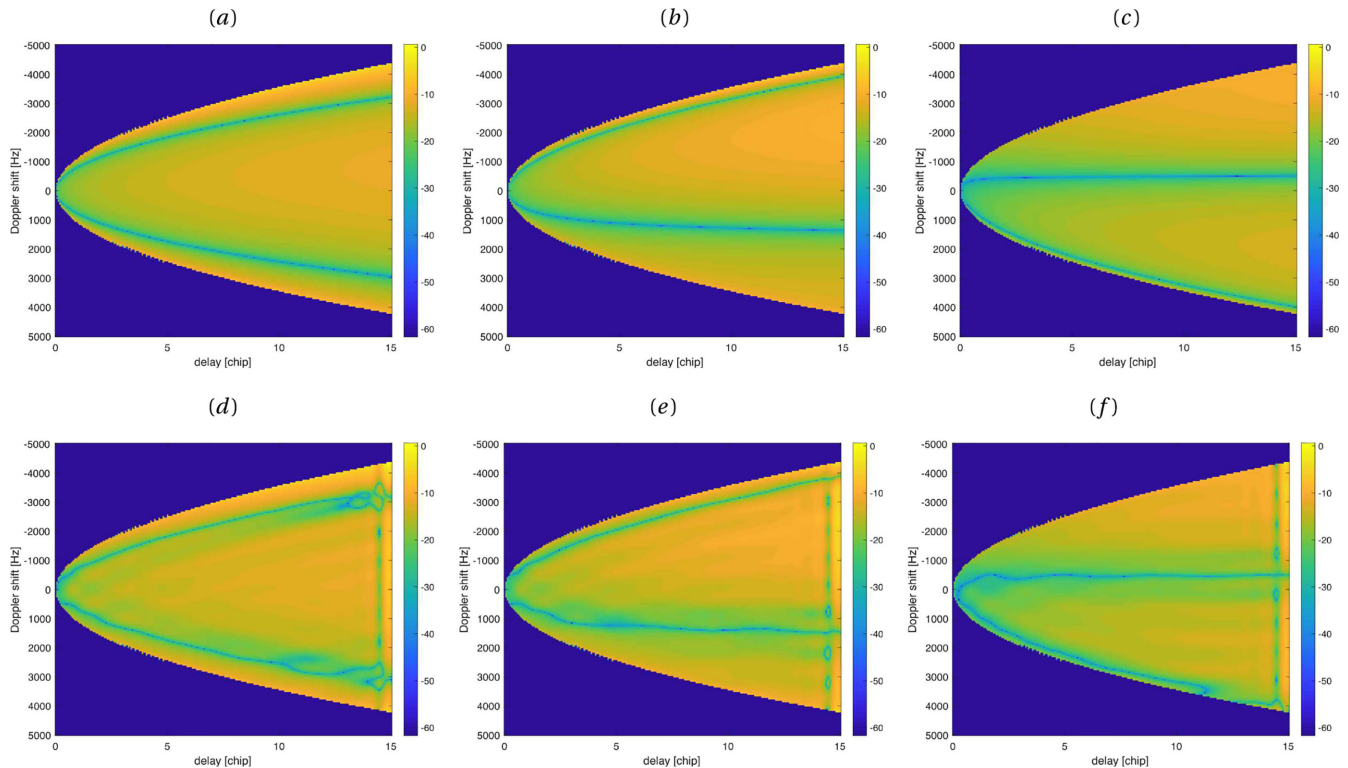
Fig. 3. Difference between SPF and SPF prototype (i.e., SPF model with 0° wind direction) in the delay–Doppler plane for several values of the wind direction and 10 m/s wind speed. (a)–(c) Differences between ideal SPF models. (d)–(f) Differences after reconstruction of the observable and prototype from parent DDMs, obtained via deconvolution and distortion correction with smoothing parameter 10^3. Wind direction is (a), (d) 30°, (b), (e) 90°, (c), (f) 120°. Colormap represents values in dB scale after normalization by a factor 10^{-15}.
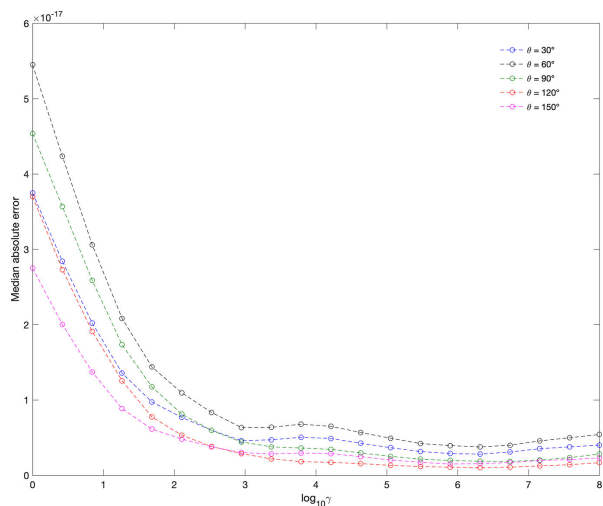

Fig. 4. Deconvolution error versus logarithm of the Lagrange multiplier.

Lagrange multiplier. From the figure, we may indicate that a fairly optimum value of the Lagrange multiplier is $\gamma = 10^3$.

IV. VALIDATION AND ASSESSMENT WITH SIMULATED DATA

A. Description of the Dataset

The DDM observables and the prototype DDMs used in this section were generated according to the stochastic model and the simulator described in [22] and [24]. The DDM observables include both speckle and thermal noise, whereas the prototype DDMs are generated according to the model in [1], i.e., speckle and thermal noise clean. Each DDM observable is produced by an incoherent average of 10^3 DDMs, each one produced with 1 ms coherent integration.

The geometric parameters were extracted from CYGNSS-01 observatory record, acquired on March 24, 2017 over the ocean surface. The SPF extends in the range $(-8000, 7950)$ Hz in Doppler and to $(0–40)$ chips in delay around the specular point and is sampled with delay–Doppler spacing of 50 Hz and 1/16 chip, respectively. After 2-D convolution, the DDM is resized such that the final observable extends from -5000 to 5000 Hz in Doppler and from -5 to 15 chips in delay.

Two datasets have been generated: Dataset A is used for performance assessment and Dataset B for validation.

1) Dataset A consists of a collection of DDMs generated using geometrical parameters from 100 equally spaced points of the selected CYGNSS track from index 1 to 100 with four values of wind speed (5, 10, 20, and 30 m/s) and five values of wind direction (30°, 60°, 90°, 120°, and 150°) for each observable. The purpose of this dataset is to provide information on variability of the wind direction estimates versus wind speed and wind direction with different acquisition geometries and signal-to-noise ratio (SNR). The SNR values for simulations along the track are shown in Fig. 5(a) for selected wind speed.
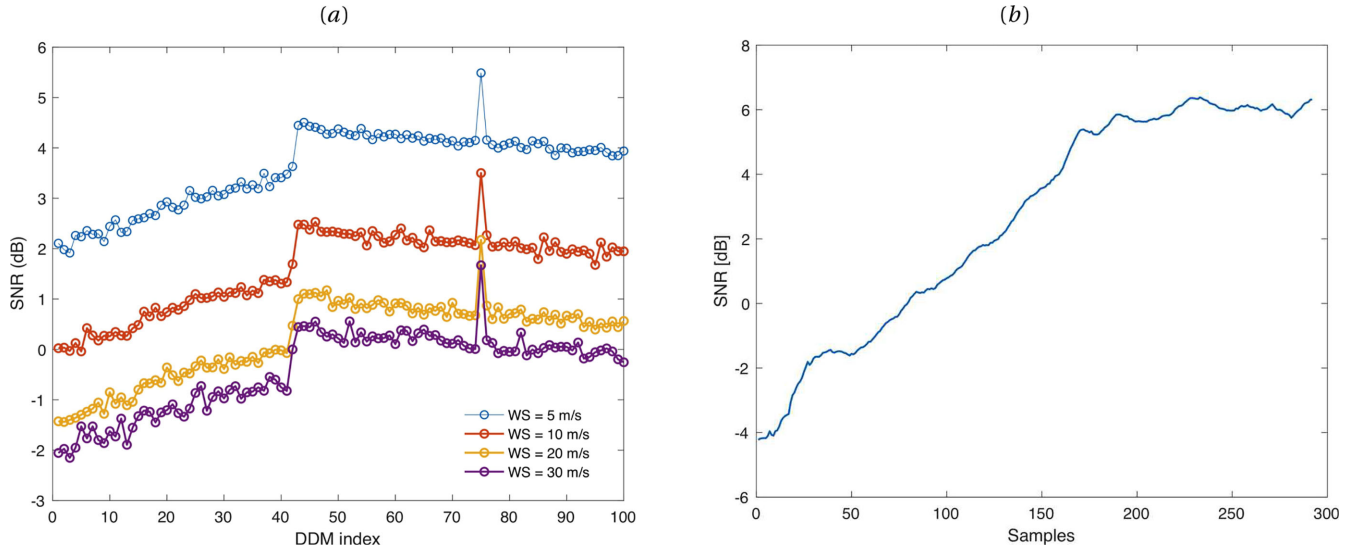
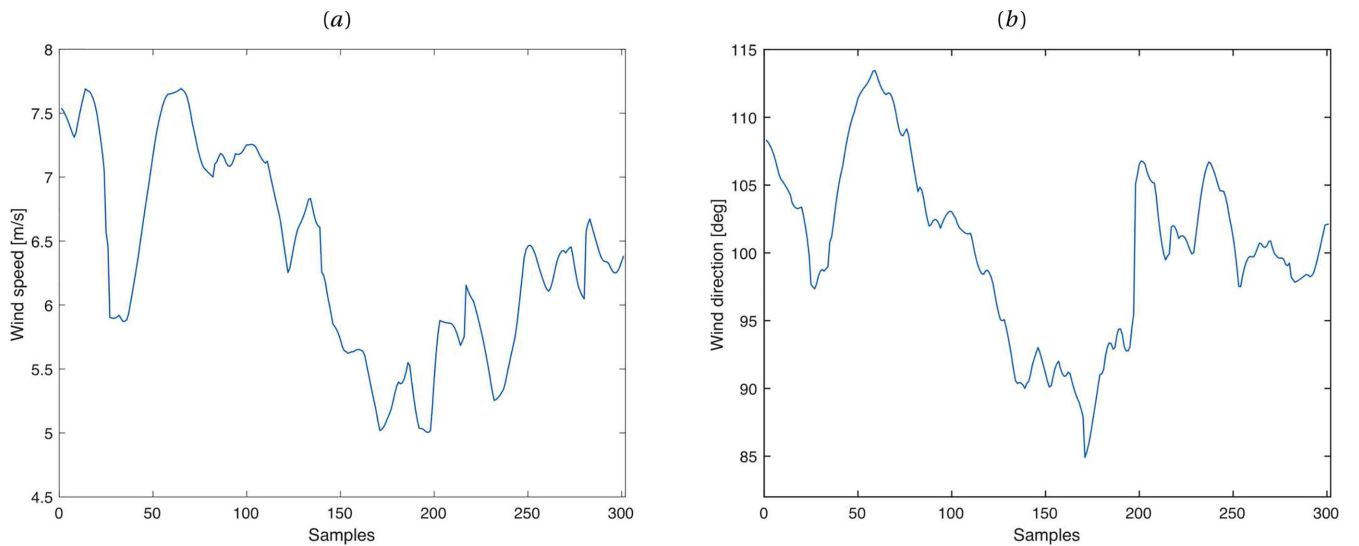Fig. 5. Estimated SNR values for DDMs in (a) dataset A and (b) dataset B.

Fig. 6. Wind speed (a) and wind direction (b) from the ECMWF collocated with CYGNSS subtrack from dataset B.

2) Dataset B consists of a collection of DDMs generated using geometrical parameters corresponding to index from 1713 to 2013, spaced 1 s, along the same CYGNSS track. In this case, the wind parameters are taken from numerical weather prediction analysis by the European Centre for Medium-Range Weather Forecasts (ECMWF) and collocated with CYGNSS track by National Oceanic and Atmospheric Administration. Wind speed ranges from 5 to 7.7 m/s and wind direction from $85°$ to $113°$, as shown in Fig. 6. The SNR values along the track are shown in Fig. 5(b). As usual, the SNR is defined as

$$\text{SNR} = 10 \log_{10} \left(\frac{P - N}{N} \right) \qquad (17)$$

where P is the maximum value of the DDM and N is the noise floor, estimated by averaging the points within a window of the DDM from -15 to -5 chips and from -5000 to 5000 Hz.

B. Performance Analysis

A first set of experiments was developed under controlled wind direction and wind speed using simulations from dataset A. Values of wind direction are in the range $0° - 180°$ because the slopes pdf is invariant to $180°$ rotation. This directional ambiguity cannot be resolved. There is a first need to investigate the performance of DNLS against LLS estimation of wind direction under variable compositions of speckle and thermal noise as well as for the ideal case where there is no speckle and thermal

TABLE I
MEAN (μ) AND STANDARD DEVIATION (σ) OF WIND-DIRECTION RETRIEVALS FOR θ SAMPLED WITH 30° SPACING

(a)

θ	WS = 5		WS = 10		WS = 20		WS = 30	
	μ	σ	μ	σ	μ	σ	μ	σ
	Ideal							
30	23.9	0.8	26.7	0.4	28.1	0.2	28.6	0.2
60	57.0	13.1	60.3	7.0	60.7	3.8	60.7	2.8
90	94.7	3.9	92.6	2.1	91.7	1.3	91.3	1.0
120	119.5	3.8	119.4	1.9	119.5	1.1	119.6	0.9
150	155.8	3.0	152.5	1.7	151.0	1.0	150.4	0.8
	Speckle noise							
30	27.1	19.9	28.6	22.2	40.0	30	37.9	28.5
60	57.7	22.9	61.1	21.9	60.0	23.1	60.2	23.0
90	88.7	26.3	92.5	26.1	86.7	30.8	85.0	30.1
120	129.4	21.8	123.5	25.9	130.6	27.3	125.2	24.1
150	153.9	16.4	154.9	16.7	147.5	22.3	149.7	21.9
	Speckle and thermal noise							
30	36.8	33.3	42.2	40.4	43.6	41.1	32.8	41.8
60	54.5	31.5	53.7	32.0	62.4	44.1	55.3	47.4
90	83.9	44.1	84.4	39.4	87.7	45.0	83.0	45.6
120	132	32.1	125.4	44.4	129.9	42.5	125.5	40.6
150	149.1	26.5	154.4	31.6	157.0	40.8	150.7	37.1

(b)

θ	WS = 5		WS = 10		WS = 20		WS = 30	
	μ	σ	μ	σ	μ	σ	μ	σ
	Ideal							
30	25.1	0.2	27.6	0.2	28.6	0.2	29.0	0.2
60	55.1	0.7	58.6	0.7	59.9	0.7	60.3	0.7
90	91.1	0.5	91.0	0.5	91.0	0.6	91.0	0.6
120	124.6	0.6	121.2	0.8	119.9	0.8	119.5	0.8
150	154.0	0.2	151.3	0.2	150.1	0.2	149.7	0.3
	Speckle noise							
30	27.5	18.2	26.5	20.9	38.1	29.4	34.7	28.6
60	56.1	19.8	62.9	19.8	62	25.1	59.3	23.7
90	88.5	22.2	92.1	23.7	90.1	29.6	87.1	29.7
120	130.1	17.3	119.8	23.1	128.3	28.1	123.4	24.1
150	155.2	14.7	156.9	17.0	147.6	24.4	151.6	24.6
	Speckle and thermal noise							
30	33.7	32.3	41.3	38.6	42.3	42.9	32.8	43.2
60	54.1	31.9	56.0	34.0	58.7	42.8	54.9	45.1
90	79.7	41.8	82.9	40.1	87.9	45.6	78.7	47.4
120	127.9	35.3	124.2	44.6	127.8	44.7	130.4	40.9
150	150.6	26.6	155.2	32.7	153.0	40.6	150.5	39.5

Values are averaged over 100 observation geometries for CYGNSS track defined in dataset A. Table (a): DNLS estimation. Table (b): LLS estimation.
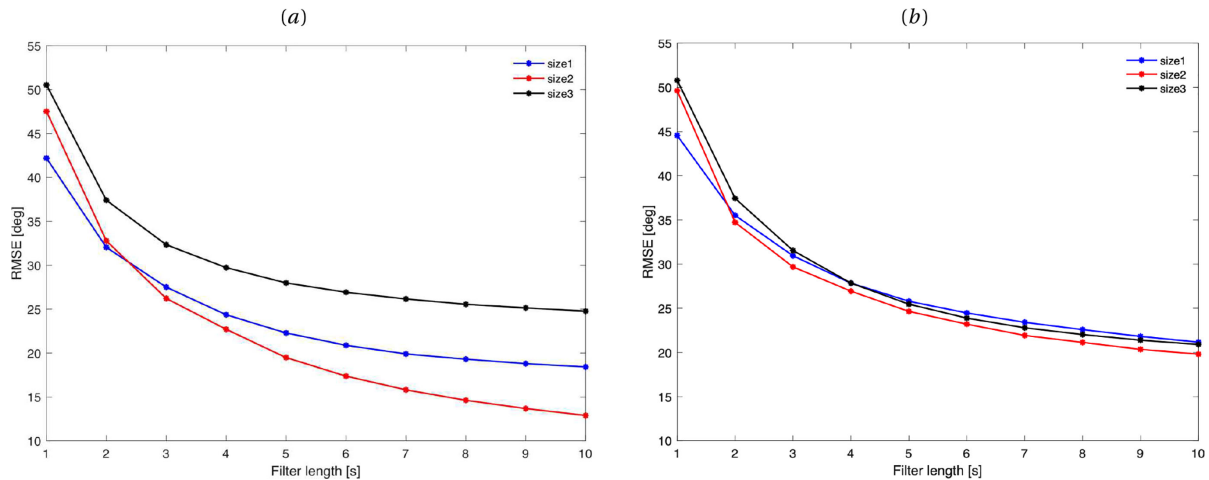

Fig. 7. RMS error between estimated and true wind direction versus length of the MA filter on (a) DNLS and (b) LLS retrievals. SPF size: size 1 ($\pm$5000 Hz for Doppler and 0–15 chips for delay, blue line), size 2 ($\pm$5000 Hz for Doppler and 0–6 chips for delay, red line), size 3 ($\pm$1000 Hz for Doppler and 0–1 chips for delay, black line).

noise. Table I lists mean and standard deviation of wind direction estimators, for several values of the wind speed (5, 10, 20, and 30 m/s) and wind direction (30°–150° with 30° spacing). Each set of 100 samples used in the averages is generated according to geometry of the selected subtrack of dataset A; all samples have the same wind speed and wind direction but different SNR values, as reported in Fig. 5(a).

Subtables (a) and (b) illustrate some interesting features of DNLS and LLS approaches. Measuring the performance of the estimation process in the absence of noise (ideal case) is of particular interest for understanding the impact of the deconvolution artifacts and pdf approximation on the wind-direction retrieval. As expected, the standard deviation of LLS estimates looks more stable than the DNLS case. It can be noticed that

for both DNLS and LLS methods the bias tends to reduce as the wind speed increases, possibly because the information related to the far region of the glistening zone is more sensitive to wind direction variations, at least in the absence of noise.

When the DDM includes speckle noise, the bias is still low enough to detect the wind direction with good accuracy, but the standard deviation increases for all values of wind speed. The two methods achieve comparable performance but values of standard deviation show large fluctuations among values of wind speed and wind direction. With thermal noise, there is a further increase of bias and standard deviation. Bias is overall higher, but for almost all estimates it remains reasonably stable with respect to wind speed.
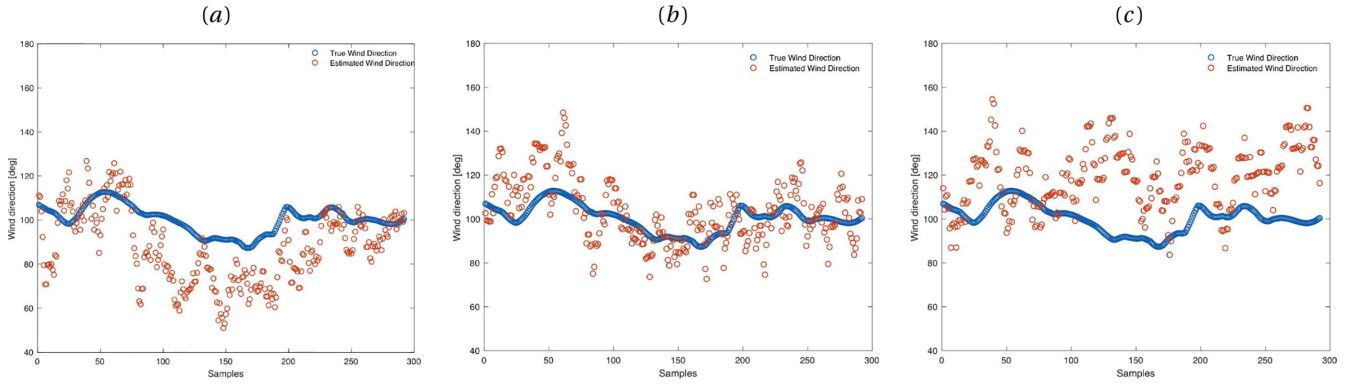
Fig. 8.   Wind-direction retrievals with DNLS inversion (brown circles) and true values (blue circles) after MA filtering for CYGNSS track defined in dataset B. The number of taps of the MA filter is 10 samples and figures refer to three different sizes of the SPF. (a) ±5000 Hz for Doppler and 0–15 chips for delay in (a). (b) ±5000 Hz for Doppler and 0–6 chips for delay. (c) ±1000 Hz for Doppler and 0–1 chips for delay.
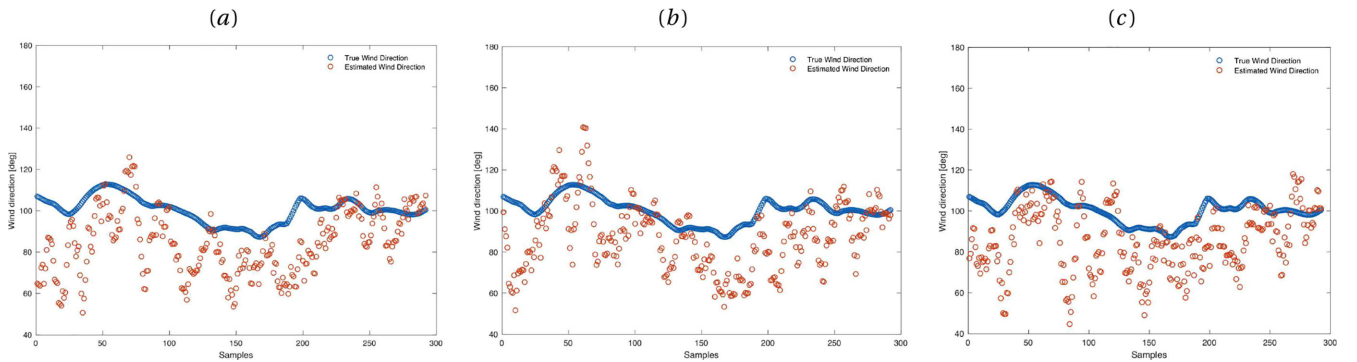

Fig. 9.   Wind-direction retrievals with LLS inversion and inverse-tangent nonlinearity (brown circles) and true values (blue circles) after MA filtering for CYGNSS track defined in dataset B. The number of taps of the filter is 10 samples and figures refer to three different sizes of the SPF. (a) ±5000 Hz for Doppler and 0–15 chips for delay in (a). (b) ±5000 Hz for Doppler and 0–6 chips for delay. (c) ±1000 Hz for Doppler and 0–1 chips for delay.

Analysis with dataset B includes a study with respect to the DDM size and realistic variations of wind speed and wind direction, as reported in Fig. 6. To following these variations, a smoothing of the estimates has been applied and Fig. 7 shows its impact on the rms error between the estimated and true wind direction. Results illustrate the effect of a moving average (MA) filter for DNLS and LLS retrievals when the length of the filter is changed from one to ten samples for three values of the SPF size: size 1 (±5000 Hz, 0–15 chips), size 2 (±5000 Hz, 0–6 chips), and size 3 (±1000 Hz, 0–1 chips). There is therefore evidence that DNLS retrieval may achieve better performance but is vulnerable to DDM size, whereas LLS is more resilient.

Wind-direction retrievals are consistent with the idea of a global robustness of LLS method that, however, may not ensure the best performance in any case, but it is slightly better than DNLS when the SPF size is small (see Fig. 7, size 3). Figs. 8 and 9 show that in almost all cases wind-direction retrievals are reasonably close to true wind directions. The performance of DNLS and LLS are comparable, but for panel (b) where DNLS exhibits smaller bias and deviation, in agreement with previous results in terms of rms error, as reported in Fig. 7, where the better quality of DNLS is quite evident for medium SPF size (size 2).

V. CONCLUSION

This study provides a first evidence that ocean wind direction can be measured with reasonable accuracy by deconvolution of DDMs received by satellite GNSS reflectometers. Simulations provide results in terms of mean and standard deviation of the estimates, useful for understanding the impact of deconvolution as well as of speckle and thermal noise. The main source of degradation for estimation accuracy is the presence of speckle and thermal noise with similar impact for the case at hand. On the other hand, deconvolution and other approximations have some impact on estimation bias. Further work can be directed to consider longer integration times across regions of the ocean surface where wind field is sufficiently smooth and to explore methods for reducing the degradation due to thermal noise. Along these lines, the following considerations arise.

1) A reliable deconvolution process requires that the DDM observable extends for at least 15 chips in delay and ±5000 Hz in Doppler, whereas standard DDMs processed on-board for CYGNSS wind speed retrievals extend for 2.5 chips in delay and ±2500 Hz in Doppler. The best choice would be to reprocess the data from raw IF sampled

signal and produce extended DDMs with high resolution (i.e., sampled with 1/16 chip sample spacing).

2) From a more general perspective, it is not strictly required that the wind direction is constant across the delay–Doppler range of values. This restriction can be relaxed allowing for a larger number of unknowns in the LS estimation with the constraint of smooth spatial variations of the solution. It is evident, from one side, a tradeoff between number of unknowns (i.e., degrees of freedom of the overdetermined system of equations) and accuracy of the solution, from the other the possibility of capturing finer variability of the wind field across the glistening zone. At the moment, the spatial resolution achieved in simulations with speckle and thermal noise using size 3, corresponds approximately to 25 km square, with rms error of $21°$ in the best case of LLS estimation and MA of ten samples. These results, if confirmed in experimental analysis with real data, would be comparable to ASCAT performance, where spatial resolution is 25 km square and the rms error, between wind direction estimation and buoy measurement, is around $18°$ [25].

3) The first validation with real data requires some amount of raw IF data collocated with measured wind fields. An initial dataset for producing experiments similar to dataset B could be composed by 300 s raw-IF acquisitions closely collocated with buoy wind direction measurements. This is compatible with usual raw IF acquisitions from CYGNSS and TDS-1 missions along planned ocean tracks.

REFERENCES

[1] V. U. Zavorotny and A. G. Voronovich, "Scattering of GPS signals from the ocean with wind remote sensing application," *IEEE Trans. Geosci. Remote Sens.*, vol. 38, no. 2, pp. 951–964, Mar. 2000.

[2] C. Ruf *et al.*, "New ocean winds satellite mission to probe hurricanes and tropical convection," *Bull. Amer. Meteorol. Soc.*, vol. 97, pp. 385–395, 2015.

[3] M. P. Clarizia and C. S. Ruf, "Wind speed retrieval algorithm for the Cyclone Global Navigation Satellite System (CYGNSS) mission," *IEEE Trans. Geosci. Remote Sens.*, vol. 54, no. 8, pp. 4419–4432, Aug. 2016.

[4] C. S. Ruf, S. Gleason, and D. S. McKague, "Assessment of CYGNSS wind speed retrieval uncertainty," *IEEE J. Sel. Topics Appl. Earth Observ. Remote Sens.*, vol. 12, no. 1, pp. 87–97, Jan. 2019.

[5] G. Foti *et al.*, "Spaceborne GNSS reflectometry for ocean winds: First results from the UK TechDemoSat-1 mission," *Geophys. Res. Lett.*, vol. 42, no. 13, pp. 5435–5441, 2015.

[6] M. Unwin, P. Jales, J. Tye, C. Gommenginger, G. Foti, and J. Rosello, "Spaceborne GNSS-reflectometry on TechDemoSat-1: Early mission operations and exploitation," *IEEE J. Sel. Topics Appl. Earth Observ. Remote Sens.*, vol. 9, no. 10, pp. 4525–4539, Oct. 2016.

[7] J. L. Garrison, A. Komjathy, V. U. Zavorotny, and S. J. Katzberg, "Wind speed measurement using forward scattered GPS signals," *IEEE Trans. Geosci. Remote Sens.*, vol. 40, no. 1, pp. 50–65, Jan. 2002.

[8] E. Valencia *et al.*, "Ocean surface's scattering coefficient retrieval by Delay-Doppler map inversion," *IEEE Geosci. Remote Sens. Lett.*, vol. 8, no. 4, pp. 750–754, Jul. 2011.

[9] H. Park, E. Valencia, N. Rodriguez-Alvarez, X. Bosch-Lluis, I. Ramos-Perez, and A. Camps, "New approach to sea surface wind retrieval from GNSS-R measurements," in *Proc. IEEE Int. Geosci. Remote Sens. Symp.*, Jul. 2011, pp. 1469–1472.

[10] G. Giangregorio, P. Addabbo, C. Galdi, and M. di Bisceglie, "Ocean wind speed estimation from the GNSS scattered power function volume," *IEEE J. Sel. Topics Appl. Earth Observ. Remote Sens.*, vol. 12, no. 1, pp. 78–86, Jan. 2019.

[11] J. L. Garrison, "Anisotropy in reflected GPS measurements of ocean winds," in *Proc. IEEE Int. Geosci. Remote Sens. Symp.*, Jul. 2003, pp. 4480–4482.

[12] C. Zuffada, T. Elfouhaily, and S. Lowe, "Sensitivity analysis of wind vector measurements from ocean reflected GPS signals," *Remote Sens. Environ.*, vol. 88, pp. 341–350, 2003.

[13] A. Komjathy, M. Armatys, D. Masters, P. Axelrad, V. Zavorotny, and S. Katzberg, "Retrieval of ocean surface wind speed and wind direction using reflected GPS signals," *J. Atmos. Ocean. Technol.*, vol. 21, no. 3, pp. 515–526, 2004.

[14] E. Valencia, V. U. Zavorotny, D. M. Akos, and A. Camps, "Using DDM asymmetry metrics for wind direction retrieval from GPS ocean-scattered signals in airborne experiments," *IEEE Trans. Geosci. Remote Sens.*, vol. 52, no. 7, pp. 3924–3936, Jul. 2014.

[15] C. Li and W. Huang, "An algorithm for sea-surface wind field retrieval from GNSS-R Delay-Doppler map," *IEEE Geosci. Remote Sens. Lett.*, vol. 11, no. 12, pp. 2110–2114, Dec. 2014.

[16] J. Park and J. T. Johnson, "A study of wind direction effects on sea surface specular scattering for GNSS-R applications," *IEEE J. Sel. Topics Appl. Earth Observ. Remote Sens.*, vol. 10, no. 11, pp. 4677–4685, Nov. 2017.

[17] D. Guan *et al.*, "Wind direction signatures in GNSS-R observables from space," *Remote Sens.*, vol. 10, no. 2, pp. 198–213, Jan. 2018.

[18] F. Wang, D. Yang, and L. Yang, "Feasibility of wind direction observation using low-altitude Global Navigation Satellite System-reflectometry," *IEEE J. Sel. Topics Appl. Earth Observ. Remote Sens.*, vol. 11, no. 12, pp. 5063–5075, Dec. 2018.

[19] R. C. Gonzalez, R. E. Woods, and S. L. Eddins, *Digital Image Processing Using MATLAB*. London, U.K.: Dorling Kindersley, 2006.

[20] C. Li, W. Huang, and S. Gleason, "Dual antenna space-based GNSS-R ocean surface mapping: Oil slick and tropical cyclone sensing," *IEEE J. Sel. Topics Appl. Earth Observ. Remote Sens.*, vol. 8, no. 1, pp. 425–435, Jan. 2015.

[21] J. F. Marchan-Hernandez, A. Camps, N. Rodriguez-Alvarez, E. Valencia, X. Bosch-Lluis, and I. Ramos-Perez, "An efficient algorithm to the simulation of Delay–Doppler maps of reflected Global Navigation Satellite System signals," *IEEE Trans. Geosci. Remote Sens.*, vol. 47, no. 8, pp. 2733–2740, Aug. 2009.

[22] P. Addabbo, G. Giangregorio, C. Galdi, and M. di Bisceglie, "Simulation of TechDemoSat-1 Delay-Doppler maps for GPS ocean reflectometry," *IEEE J. Sel. Topics Appl. Earth Observ. Remote Sens.*, vol. 10, no. 9, pp. 4256–4268, Sep. 2017.

[23] M. P. Clarizia and C. S. Ruf, "On the spatial resolution of GNSS reflectometry," *IEEE Geosci. Remote Sens. Lett.*, vol. 13, no. 8, pp. 1064–1068, Aug. 2016.

[24] G. Giangregorio, M. di Bisceglie, P. Addabbo, T. Beltramonte, S. D'Addio, and C. Galdi, "Stochastic modeling and simulation of Delay-Doppler maps in GNSS-R over the ocean," *IEEE Trans. Geosci. Remote Sens.*, vol. 54, no. 4, pp. 2056–2069, Apr. 2016.

[25] A. Bentamy, D. Croize-Fillon, and C. Perigaud, "Characterization of ASCAT measurements based on buoy and QuikSCAT wind vector observations," *Ocean Sci.*, vol. 4, no. 4, pp. 265–274, 2008.

Generoso Giangregorio was born in Benevento, Italy, in 1981. He received the M.S. degree in telecommunications engineering (*summa cum laude*) and Ph.D. degree in information engineering from the Università degli Studi del Sannio, Benevento, Italy, in 2007 and 2012, respectively.

Since 2012, he has been a Research Fellow with the Telecommunications and Remote Sensing Group, Università degli Studi del Sannio. His research interests include satellite image processing, transmission data techniques, and Global Navigation Satellite System reflectometry.

Carmela Galdi (Member, IEEE) received the Dr.Eng. and Ph.D. degrees in electronic engineering from the Università degli Studi di Napoli Federico II, Naples, Italy, in 1992 and 1997, respectively.

In 1995, she spent a period for study and research with the Signal Processing Division, University of Strathclyde, Glasgow, U.K. In 1997, she was a Visiting Scientist with the University College of London, London, U.K., and with the Defense Evaluation and Research Agency, Malvern, U.K, working on statistical models of radar backscattering from natural surfaces. In 2000, she joined the Università degli Studi del Sannio, Benevento, Italy, where she is currently a Professor in Telecommunications. She has cooperated with the National Oceanography Centre, Southampton, U.K., on a project about GNSS-R of the ocean surface. She is currently associated with the NASA CYGNSS project as an external science team member, working on statistical models for GNSS-R signals in different ocean conditions and on retrieval of wind field from delay-Doppler maps. Her research interests include statistical signal processing, non-Gaussian models of radar backscattering, and Global Navigation Satellite System Reflectometry.

Maurizio di Bisceglie (Member, IEEE) was born in Naples, Italy. He received the Ph.D. degree in electronic and communications engineering from Università degli Studi di Napoli "Federico II," Naples, Italy, in 1993.

Since 1998, he has been with the Università degli Studi del Sannio, Benevento, Italy, as an Associate Professor of Telecommunications. He was a Visiting Scientist with the University College of London, London, U.K. and with the Defense Evaluation and Research Agency, Malvern, U.K. His research interests include statistical signal processing with applications to stochastic modeling and GNSS reflectometry.

Dr. di Bisceglie was with the organizing committee of the Italian phase of European AQUA Thermodynamic Experiment mission, in 2004, Co-Chair of the NASA Direct Readout Conference, in 2005, and with the organizing committee of the IEEE 2008 Radar Conference. Since 2016, he has been a member of the NASA CYGNSS external science team.